J. Fluid Mech. (2002), *vol.* 470, *pp.* 151–179.
DOI: 10.1017/S0022112002001702 Printed in the United Kingdom

Linear optimal control applied to instabilities in spatially developing boundary layers

By MARKUS HÖGBERG[1,2] AND DAN S. HENNINGSON[1,2]

[1]Department of Mechanics, Royal Institute of Technology, Stockholm, Sweden

[2]The Swedish Defense Research Agency (FOI), SE-172 90, Stockholm, Sweden

(Received 3 September 2001 and in revised form 10 April 2002)

The work presented extends previous research on linear controllers in temporal channel flow to spatially evolving boundary layer flow. The flows studied are those on an infinite swept wedge described by the Falkner–Skan–Cooke (FSC) velocity profiles, including the special case of the flow over a flat plate. These velocity profiles are used as the base flow in the Orr–Sommerfeld–Squire equations to compute the optimal feedback control through blowing and suction at the wall utilizing linear optimal control theory. The control is applied to a parallel FSC flow with unstable perturbations. Through an eigenvalue analysis and direct numerical simulations (DNS), it is shown that instabilities are stabilized by the controller in the parallel case. The localization of the convolution kernels for control is also shown for the FSC profiles.

Assuming that non-parallel effects are small a technique is developed to apply the same controllers to a DNS of a spatially evolving flow. The performance of these controllers is tested in a Blasius flow with both a Tollmien–Schlichting (TS) wave and an optimal spatial transiently growing perturbation. It is demonstrated that TS waves are stabilized and that transient growth is lowered by the controller. Then the control is also applied to a spatial FSC flow with unstable perturbations leading to saturated cross-flow vortices in the uncontrolled case. It is demonstrated that the linear controller successfully inhibits the growth of the cross-flow vortices to a saturated level and thereby delays the possibility of transition through secondary instabilities. It is also demonstrated that the controller works for relatively high levels of nonlinearity, and for stationary as well as time-varying perturbations.

1. Introduction

In many fluid-mechanics systems, like boundary layers undergoing transition to turbulence, a dramatic effect on global flow parameters may be achieved by minute local perturbations. Whereas such a fundamental instability property is a problem in many applications, it can be the basis for dramatic performance improvements of fluid-mechanics systems using devices sensing and acting only on small parts of the flow with minute energy. Such control devices could be used to obtain drag reduction on bodies, increased lift on wings, increased propulsion efficiency, heat- and mass-transfer reduction or enhancement, control of combustion instabilities, control of vortex shedding and aeroacoustic pressure fluctuations.

Recent advances in computer capacity, sensor development and systems control for fluid dynamics have opened new possibilities for the design and control of flow systems (see for instance the review articles of Gad-el-Hak 1996; Lumley & Blossey 1998 and Bewley 2001). Worldwide this area has seen a strong expansion over the last few years.

Traditionally passive control, i.e. design or flow alteration not dynamically dependent on the state of the flow, has been used to control fluid-mechanical systems. Active control of boundary layers is a more recent development, where e.g. transition has been delayed by cancelling Tollmien–Schlichting (TS) waves by anti-phase modal suppression. Early work is reviewed by Thomas (1990) and a brief later review is given by Metcalfe (1994). These studies show that the instabilities may indeed be significantly suppressed, but complete elimination of the primary disturbances is not obtained.

Researchers have only recently attempted to apply optimal-control ideas to flow control problems. A main feature of such an approach is that no *a priori* knowledge of the functional behaviour of an effective control is needed. Also, the method is general; it can be used for such disparate tasks as finding the optimal shapes of wings (Jameson 1989), minimizing the vorticity of an unsteady internal flow by manipulating the inlets (Berggren 1995), as well as controlling boundary-layer transition (Joslin *et al.* 1997) and turbulence (Bewley, Moin & Temam 2001). In addition, optimal control based on linearized equations has shown great success in recent applications to channel flow (see Joshi, Speyer & Kim 1997; Bewley & Liu 1998; Högberg & Bewley 2000 or Högberg, Bewley & Henningson 2002). In this approach modern linear control theory is used to construct feedback control kernels as well as estimator forcing kernels, which can be used together as an on-line compensator. In Högberg *et al.* (2002) it is demonstrated that the convolution kernels obtained through this approach are localized, meaning that their tails decay exponentially a finite distance from the origin. This implies that the state information utilized by the optimal controller is only that in the neighbourhood of the actuator. The implications of this localization property for physical implementation of these controllers is discussed thoroughly in Bewley (2001).

Control of transition in boundary layer flows has numerous application areas, but so far there has been little use made of active control strategies in practice. Experimentally control has been applied to boundary layer flows using both passive and active strategies, utilizing many different means of actuation. A complete review is not given here but, rather, a few examples to give a flavour of the activities in this field. Passive strategies include using riblets and surface roughness to modify the flow. A thorough study on the use of riblets to suppress the intensity of streamwise vortices in boundary layers is summarized by Kozlov & Grek (2000). Using passive control, Saric, Carrillo & Reibert (1998) showed that it was possible to use leading-edge roughness for transition control in order to delay transition by exploiting the nonlinear nature of the flow. To use this method in a general case an actuation method was developed by White & Saric (2000) who introduced a variable surface roughness at the leading edge of a swept wing to actively control transition initiated by cross-flow vortices. The success of generalizing the passive control scheme into an active one relies on a better understanding of the transition process, especially the role of secondary instabilities. The breakdown of a localized disturbance into a turbulent spot in a flat-plate boundary layer was successfully delayed using active wall bumps by Breuer, Haritonidis & Landahl (1989). An active strategy to control streamwise vortices and streaks in boundary layers was applied by Jacobson & Reynolds (1998). They developed an actuator that produces a high- and a low-speed streak that was used to delay transition. The use of these active control strategies in a practical feedback control scheme relies, in addition to a good physical understanding of the transition process, on development of accurate sensors and actuators.

As an alternative to experiments, computations can be used to investigate what is possible to achieve under ideal conditions, as well as to test new strategies. Active control of cross-flow vortices related to the aforementioned work by Saric *et al.* (1998) has been studied numerically by Wassermann & Kloker (2000) where an out-of-phase type control was applied to cross-flow vortex packets using direct numerical simulation (DNS). They found that a modal control, where the phase shift of the control was adjusted individually for different modes, was necessary to achieve an effective total amplitude reduction. Cathalifaud & Luchini (2000) applied an optimal control technique to the boundary layer equations to control optimal spatially developing perturbations in the boundary layer on a flat or concave wall. They used the adjoint equations to perform a gradient-based optimization with the objective of minimizing the perturbation energy in different spatial intervals. Mughal (1998) used the compressible parabolized stability equations (PSE) to investigate the effect of simple feedback boundary conditions for the wall-normal velocity to control for example TS-waves and Görtler vortices. In recent work Pralits, Hanifi & Henningson (2001) have developed a method to couple the boundary layer equations and the PSE in order to optimize a steady mean-flow-modifying suction in order to minimize growth of perturbations in boundary layer flows. Walther, Airiau & Bottaro (2001) used PSE to compute the optimal zero mass flux control for a TS wave in a developing boundary layer. A slightly different approach was investigated by Balakumar & Hall (1999) where an optimization problem coupling the boundary layer equations and the linear stability equations was solved with the objective of moving the transition point instead of minimizing the perturbation energy. The numerical approaches to flow control often assume ideal conditions that are not present in practice. Robust control schemes are vital in order to make the step from computers to the experimental setting and to practical applications.

In the present paper the linear control approach from Högberg & Bewley (2000) and Högberg *et al.* (2002) is applied to spatially evolving boundary layer flows to investigate whether a linear controller developed for a parallel flow also provides stability in a non-parallel flow. In § 2.1 the Falkner–Skan–Cooke (FSC) boundary layer profiles are introduced and then the formulation of the linear control problem is presented in § 2.2. The solution procedure for the optimal control problem is outlined in § 2.3 and the extension to spatially developing boundary layers is explained in § 2.4. Numerical issues regarding the computation of the feedback controllers is presented in § 3.1, and descriptions of the numerical simulations performed and the methods used are given in § 3.2. In § 4 the linear optimal control is applied to a parallel FSC flow in order to explain some features of the control as well as to validate the control strategy and the numerical implementation. Results from simulations with and without control in spatially developing boundary layers are presented in § 5 for the Blasius boundary layer and in § 6 for the FSC boundary layer for non-stationary as well as stationary perturbations. Finally a discussion and conclusion follow in § 7.

2. Linear control theory

2.1. *Falkner–Skan–Cooke boundary layers*

We start by introducing the mean-flow profiles to be used for linearization of the Navier–Stokes equations. The Falkner–Skan–Cooke boundary layer profile family includes a large variety of flows. It includes the Blasius boundary layer as a special

case, and the effect of sweep and favourable/adverse pressure gradients can be added. These different flows have been studied previously and are known to exhibit different types of primary instabilities. In order to test the control strategy for different types of instabilities we need to examine its effectiveness in a few different flows.

We assume that the chordwise base flow at the boundary layer edge obeys a power law according to $U^*_\infty = U^*_0(x^*/x^*_0)^m$ and that $W^*_\infty = \text{constant}$. Note that the asterisk ($*$) usually denotes a complex conjugate transpose, but here it is used to denote dimensional variables. A self-similar solution may be found from the boundary layer equations if we select

$$\eta = \{(m+1)U^*_\infty/2\nu x^*\}^{1/2} y^*. \tag{2.1}$$

Using a stream-function formulation, the equations for the self-similar boundary layer profiles can be derived (see e.g. Schlichting 1979),

$$f''' + ff'' + \beta_H(1 - f'^2) = 0, \tag{2.2}$$

$$g'' + fg' = 0, \tag{2.3}$$

where the Hartree parameter is $\beta_H = 2m/(m+1)$ and the boundary conditions are

$$f = f' = g = 0 \quad \text{for} \quad \eta = 0, \tag{2.4}$$

$$f' \to 1, \quad g \to 1 \quad \text{as} \quad \eta \to \infty. \tag{2.5}$$

The solutions f' and g can then be combined into the Falkner–Skan–Cooke velocity profiles, see Cooke (1950), as

$$U(y) = f'[\eta(y)], \tag{2.6}$$

$$W(y) = \frac{W^*_\infty}{U^*_\infty} g[\eta(y)], \tag{2.7}$$

with $y = y^*/\delta^*_0$ and

$$\eta(y) = \left(\int_0^\infty (1 - f')\,\mathrm{d}\eta \right) \left\{ \frac{U^*_\infty x^*_0}{U^*_0 x^*} \right\}^{1/2} y,$$

where x^*_0 is a fixed position and U^*_0 is the free-stream velocity at that position. The profiles (2.6) and (2.7) will be used as a base flow in the control computations and as initial conditions in the direct numerical simulations presented.

2.2. *Control problem formulation*

To investigate the stability of a flow to small disturbances, we assume that the flow can be divided into two parts:

$$\boldsymbol{u} = (u, v, w) = (U, 0, W) + (u', v', w'), \tag{2.8}$$

where U and W are the base flow components in the chordwise and spanwise directions, respectively. The coordinate system and base flow velocity profiles are illustrated in figure 1. It is here assumed that the parallel flow assumption holds, i.e. the base flow components only vary with the normal coordinate. The primed quantities represent a small perturbation. We also assume wave-like disturbances of the form

$$u' = \hat{u}(y, t)\, \mathrm{e}^{\mathrm{i}(\alpha x + \beta z)}, \tag{2.9}$$

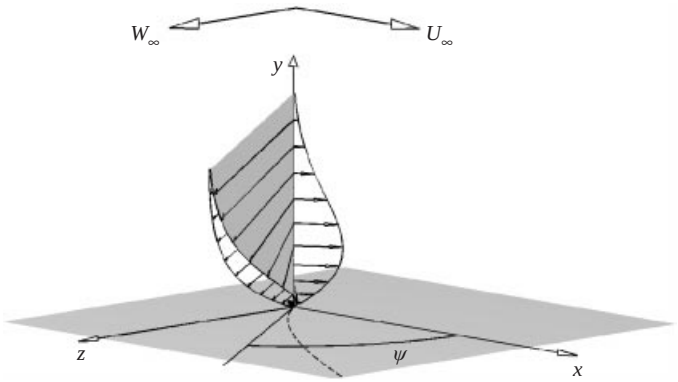

FIGURE 1. Falkner–Skan–Cooke base flow and coordinate system used in this report. ψ is the angle with the streamline of the flow in the free-stream, U_∞ is the chordwise free-stream component and W_∞ is the spanwise free-stream component. The dashed line is the streamline of the flow in the free-stream over a flat plate with a pressure gradient in the x-direction.

where α and β are the x- and z-components of the wavenumber vector and $\hat{u}(y,t)$ is the complex amplitude function for the corresponding velocity. Inserting these assumptions into the Navier–Stokes equations and linearizing, we find the resulting disturbance equations, which can be reduced to the following set of two coupled equations where appropriate boundary conditions have been included to allow inversion of the Laplacian ($\Delta = (\mathrm{D}^2 - \alpha^2 - \beta^2)$):

$$\frac{\mathrm{d}\hat{v}}{\mathrm{d}t} = \underbrace{\Delta^{-1}\left[-(\mathrm{i}\,\alpha\,U + \mathrm{i}\,\beta\,W)\Delta + \mathrm{i}\,\alpha\,D^2U + \mathrm{i}\,\beta\,D^2W + \frac{1}{R}\Delta^2\right]}_{\mathscr{L}_{OS}}\hat{v}, \tag{2.10}$$

$$\frac{\mathrm{d}\hat{\eta}}{\mathrm{d}t} = \underbrace{[\mathrm{i}\,\alpha\,DW - \mathrm{i}\,\beta\,DU]}_{\mathscr{L}_C}\hat{v} + \underbrace{\left[-\mathrm{i}\,(\alpha\,U + \beta\,W) + \frac{1}{R}\Delta\right]}_{\mathscr{L}_{SQ}}\hat{\eta}, \tag{2.11}$$

where $\hat{v}$ and $\hat{\eta} = \mathrm{i}(\beta\hat{u} - \alpha\hat{w})$ are the amplitude functions for the normal velocity and the normal vorticity, respectively. D denotes the derivative operator in the wall-normal direction. The boundary conditions are

$$\begin{aligned} &\hat{v}(0,t) = \hat{\varphi}, \quad \mathrm{D}\hat{v}(0,t) = 0, \quad \hat{\eta}(0,t) = 0, \\ &\hat{v}(y,t) \to 0, \quad \mathrm{D}\hat{v}(y,t) \to 0, \quad \hat{\eta}(y,t) \to 0 \quad \text{as} \quad y \to \infty. \end{aligned} \tag{2.12}$$

Here R is the Reynolds number based on the velocity scale U_∞ and the displacement thickness δ^*, both taken at the streamwise location x_0. The normal velocity on the wall $\hat{v}(0,t) = \hat{\varphi}$ is our control input to the system. Re will be used to denote the Reynolds number based on local displacement thickness and free-stream velocity.

Equation (2.10) is referred to as the Orr–Sommerfeld equation, and (2.11) is known as the Squire equation. The $U(y)$ and $W(y)$ profiles used in this investigation are taken from (2.6) and (2.7) in the previous subsection. Since (2.10) and (2.11) is a linear system of equations we can divide the solution into one homogeneous $(\hat{v}_h, \hat{\eta}_h)$

and one inhomogeneous $(\hat{v}_p, \hat{\eta}_p)$ part such that,

$$\underbrace{\begin{bmatrix} \hat{v} \\ \hat{\eta} \end{bmatrix}}_{\hat{\boldsymbol{x}}_f} = \underbrace{\begin{bmatrix} \hat{v}_h \\ \hat{\eta}_h \end{bmatrix}}_{\hat{\boldsymbol{x}}_h} + \underbrace{\begin{bmatrix} \hat{v}_p \\ \hat{\eta}_p \end{bmatrix}}_{\hat{\boldsymbol{Z}}} \hat{\varphi}, \tag{2.13}$$

where the conditions on the particular solution are such that it satisfies the boundary condition (2.12) with $\hat{\varphi} = 1$. Finding a particular solution with non-zero normal velocity on the wall allows us to parameterize the inhomogeneous part of the solution with the time derivative of the wall-normal velocity:

$$\frac{\mathrm{d}}{\mathrm{d}t}\begin{bmatrix} \hat{v} \\ \hat{\eta} \end{bmatrix} = \underbrace{\begin{bmatrix} \mathscr{L}_{OS} & 0 \\ \mathscr{L}_C & \mathscr{L}_{SQ} \end{bmatrix}}_{\boldsymbol{N}} \begin{bmatrix} \hat{v} \\ \hat{\eta} \end{bmatrix} \Rightarrow \dot{\hat{\boldsymbol{x}}}_h = \boldsymbol{N}\hat{\boldsymbol{x}}_h + \boldsymbol{N}\hat{\boldsymbol{Z}}\hat{\varphi} - \hat{\boldsymbol{Z}}\dot{\hat{\varphi}}, \tag{2.14}$$

with the boundary conditions,

$$\hat{v}_h(0,t) = 0, \quad \mathrm{D}\hat{v}_h(0,t) = 0, \quad \hat{\eta}_h(0,t) = 0, \tag{2.15}$$

$$\hat{v}_h(y,t) \to 0, \quad \mathrm{D}\hat{v}_h(y,t) \to 0, \quad \hat{\eta}_h(y,t) \to 0 \quad \text{as} \quad y \to \infty. \tag{2.16}$$

Now control theory can be used to determine $\dot{\hat{\varphi}}$ from $\hat{\boldsymbol{x}}_h$. Introducing $\hat{\boldsymbol{x}} = [\hat{\boldsymbol{x}}_h, \hat{\varphi}]^T$ we can write

$$\dot{\hat{\boldsymbol{x}}} = \boldsymbol{A}\hat{\boldsymbol{x}} + \boldsymbol{B}\dot{\hat{\varphi}}, \quad \text{where} \quad \boldsymbol{A} = \begin{bmatrix} \boldsymbol{N} & \boldsymbol{N}\hat{\boldsymbol{Z}} \\ 0 & 0 \end{bmatrix}, \quad \boldsymbol{B} = \begin{bmatrix} -\hat{\boldsymbol{Z}} \\ 1 \end{bmatrix}. \tag{2.17}$$

One very important issue is to determine in what sense the controller should be optimal. Our goal of preventing transition does not easily translate into a quadratic measure of the state to be minimized, and the question of what the 'optimal' objective is remains open. Here the choice is to minimize the perturbation energy, although other options might also be justified from physical arguments. The objective function used is

$$J = \int_0^T (\hat{\boldsymbol{x}}^* \boldsymbol{Q} \hat{\boldsymbol{x}} + \ell^2 \dot{\hat{\varphi}}^* \dot{\hat{\varphi}})\,\mathrm{d}t, \tag{2.18}$$

where $\boldsymbol{Q}$ is a measure of the energy of the perturbation and ℓ is a parameter penalizing the magnitude of $\dot{\hat{\varphi}}$. For each wavenumber pair $\boldsymbol{Q}$ can be written,

$$\boldsymbol{Q} = \begin{bmatrix} \mathscr{Q} & \mathscr{Q}\boldsymbol{Z} \\ \boldsymbol{Z}^*\mathscr{Q} & (1+r^2)\boldsymbol{Z}^*\mathscr{Q}\boldsymbol{Z} \end{bmatrix}, \tag{2.19}$$

where $\mathscr{Q}$ is such that

$$\hat{\boldsymbol{x}}_f^* \mathscr{Q} \hat{\boldsymbol{x}}_f = \frac{1}{y_\infty}\int_0^{y_\infty} \hat{\boldsymbol{x}}_f^* \mathscr{C}_1^* \mathscr{C}_1 \hat{\boldsymbol{x}}_f \mathrm{d}y = \frac{1}{4\,y_\infty k^2}\int_0^{y_\infty} \left(\frac{\partial \hat{v}}{\partial y}^* \frac{\partial \hat{v}}{\partial y} + k^2 \hat{v}^* \hat{v} + \hat{\eta}^* \hat{\eta} \right) \mathrm{d}y, \tag{2.20}$$

with $k^2 = \alpha^2 + \beta^2$. The parameter r^2 is used to add an extra penalty on $\hat{\varphi}^2$ in addition to the natural penalization obtained through the lifting.

2.3. *Solution procedure for the optimal control problem*

The optimal controller is given through the solution of the optimization problem; find $\dot{\hat{\phi}}$ that minimizes the objective function (2.18) subject to

$$\dot{\hat{\boldsymbol{x}}} = \boldsymbol{A}\hat{\boldsymbol{x}} + \boldsymbol{B}\,\dot{\hat{\phi}}, \quad \hat{\boldsymbol{x}}(t=0) = \hat{\boldsymbol{x}}_0. \tag{2.21}$$

A heuristic summary of the solution procedure for the optimal control problem follows. Taking the first variation with respect to the state and the control of equation (2.21) and the objective function (2.18) we can in the inner product,

$$\langle f, g\rangle = \frac{1}{y_\infty}\int_0^T \int_0^{y_\infty} f^* g \,\mathrm{d}y\,\mathrm{d}t, \quad \langle f, \boldsymbol{H}g\rangle = \langle \boldsymbol{H}^* f, g\rangle + \text{boundary terms},$$

derive the corresponding adjoint equation. Using the adjoint identity we can manipulate the inner product of $\hat{\boldsymbol{p}}(y,t)$ and the first variation of the state equation such that

$$\langle \hat{\boldsymbol{p}},\, \delta\dot{\hat{\boldsymbol{x}}} - \boldsymbol{A}\hat{\boldsymbol{x}} - \boldsymbol{B}\,\delta\dot{\hat{\phi}}\rangle = \langle -\dot{\hat{\boldsymbol{p}}} - \boldsymbol{A}^*\hat{\boldsymbol{p}}, \delta\hat{\boldsymbol{x}}\rangle - \langle \boldsymbol{B}^*\hat{\boldsymbol{p}},\, \delta\dot{\hat{\phi}}\rangle + \text{boundary terms} = 0. \tag{2.22}$$

By introducing the adjoint equation,

$$-\dot{\hat{\boldsymbol{p}}} = \boldsymbol{A}^*\hat{\boldsymbol{p}} + \mathscr{C}_1^*\mathscr{C}_1\hat{\boldsymbol{x}}, \quad \hat{\boldsymbol{p}}(y,T) = 0, \tag{2.23}$$

into (2.22) and combining with the first variation of the objective function we obtain

$$\delta J = \langle \mathscr{C}_1^*\mathscr{C}_1\hat{\boldsymbol{x}}, \delta\hat{\boldsymbol{x}}\rangle + \ell^2\langle \dot{\hat{\phi}}, \delta\dot{\hat{\phi}}\rangle = \langle \boldsymbol{B}^*\hat{\boldsymbol{p}} + \ell^2\dot{\hat{\phi}}, \delta\dot{\hat{\phi}}\rangle.$$

One can then show by setting $\delta J = 0$ that the optimal feedback law is given by

$$\dot{\hat{\phi}} = -\frac{1}{\ell^2}\boldsymbol{B}^*\hat{\boldsymbol{p}}. \tag{2.24}$$

By introducing the linear mapping $\hat{\boldsymbol{p}} = \hat{\boldsymbol{X}}\hat{\boldsymbol{x}}$ and (2.24) into equations (2.21) and (2.23) one can derive the stationary operator Riccati equation by letting $T \to \infty$ in (2.18),

$$\left(\hat{\boldsymbol{X}}\,\boldsymbol{A} + \boldsymbol{A}^*\,\hat{\boldsymbol{X}} - \frac{1}{\ell^2}\hat{\boldsymbol{X}}\,\boldsymbol{B}\boldsymbol{B}^*\,\hat{\boldsymbol{X}} + \mathscr{C}_1^*\mathscr{C}_1\right)\hat{\boldsymbol{x}} = 0, \quad \forall\hat{\boldsymbol{x}}. \tag{2.25}$$

For details on properties of this type of equation the reader is referred to e.g. Ito & Morris (1998) and Hulsing (1999). The optimal feedback control law $\dot{\hat{\phi}} = \hat{\boldsymbol{K}}\hat{\boldsymbol{x}}$ can now be found through the expression $\hat{\boldsymbol{K}} = -(1/\ell^2)\boldsymbol{B}^*\hat{\boldsymbol{X}}$ where $\hat{\boldsymbol{X}}$ is the non-negative self-adjoint solution to (2.25). Applying this feedback control gives us the closed loop system

$$\dot{\hat{\boldsymbol{x}}} = \underbrace{(\boldsymbol{A} + \boldsymbol{B}\hat{\boldsymbol{K}})}_{\boldsymbol{A}_{cl}}\hat{\boldsymbol{x}}, \tag{2.26}$$

where A_{cl} describes the dynamics of the controlled system. Dividing $\hat{\boldsymbol{K}}$ into three parts such that $\hat{\boldsymbol{K}}\hat{\boldsymbol{x}} = \hat{\boldsymbol{K}}_{\hat{v}}\,\hat{v}_h + \hat{\boldsymbol{K}}_{\hat{\eta}}\,\hat{\eta}_h + \hat{K}_{\hat{\phi}}\,\hat{\phi}$, the contribution from the normal velocity and the normal vorticity can be studied separately. To obtain the feedback operator for the inhomogeneous flow we need to remove the contribution from the inhomogeneous part of the flow from the feedback operator using (2.13):

$$\dot{\hat{\phi}} = \hat{\boldsymbol{K}}_{\hat{v}}\,\hat{v}_h + \hat{\boldsymbol{K}}_{\hat{\eta}}\,\hat{\eta}_h + \hat{K}_{\hat{\phi}}\,\hat{\phi} = \hat{\boldsymbol{K}}_{\hat{v}}\,\hat{v} + \hat{\boldsymbol{K}}_{\hat{\eta}}\,\hat{\eta} + \underbrace{(\hat{K}_{\hat{\phi}} - \hat{\boldsymbol{K}}_{\hat{v}}\,\hat{v}_p - \hat{\boldsymbol{K}}_{\hat{\eta}}\,\hat{\eta}_p)}_{\hat{\mathscr{K}}_{\hat{\phi}}}\,\hat{\phi}. \tag{2.27}$$

We can now define the final expression for the feedback operator for the inhomogeneous flow for one wavenumber pair:

$$\hat{\boldsymbol{K}}(\alpha,\beta) = [\hat{\boldsymbol{K}}_{\hat{v}}, \hat{\boldsymbol{K}}_{\hat{\eta}}, \hat{\mathscr{K}}_{\hat{\phi}}]. \tag{2.28}$$

Utilizing the Riesz Representation theorem, the operators can be expressed as integration kernels in the normal direction,

$$\dot{\hat{\phi}} = \hat{\boldsymbol{K}}\hat{\boldsymbol{x}}_f = \int_0^{y_\infty} \hat{\boldsymbol{k}}(y)\,\hat{\boldsymbol{x}}_f(y)\,\mathrm{d}y. \tag{2.29}$$

An alternative, more direct, approach is to solve for the integration kernel ($\hat{\boldsymbol{k}}$) using Chandrasekhar equations as described in e.g. Hulsing (1999). By solving for $\hat{\boldsymbol{k}}$ all wavenumber pairs (α, β) and combining these we can inverse Fourier transform the combined controllers. Since the feedback law is described by products in Fourier space, convolution integrals are obtained in physical space. Denoting the different components of the physical-space feedback kernel $\boldsymbol{k}$ by k_v, k_η and k_φ respectively, the feedback law in physical space is

$$\begin{aligned}\dot{\varphi}(x,z,t) = \int_\Omega &(k_v(x-\bar{x},y,z-\bar{z})\,v'(\bar{x},y,\bar{z},t)\\ &+ k_\eta(x-\bar{x},y,z-\bar{z})\,\eta'(\bar{x},y,\bar{z},t))\,\mathrm{d}\bar{x}\,\mathrm{d}y\,\mathrm{d}\bar{z}\\ &+ \int_\Gamma k_\varphi(x-\bar{x},z-\bar{z})\,\varphi(\bar{x},\bar{z},t)\,\mathrm{d}\bar{x}\,\mathrm{d}\bar{z},\end{aligned} \tag{2.30}$$

where Ω denotes the inner part of the domain and Γ is the wall. Figure 2(c) shows isosurfaces of the convolution kernel in physical space for the v velocity, and figure 2(a) shows contour plots of the same kernel. In figure 2(b) the two-dimensional kernel for φ representing the feedback of the blowing and suction velocity applied is shown as a contour plot. The convolution kernel for η is visualized in figures 3(a) and 3(b). These kernels are computed at $x = 50$ in a box with the dimensions $100 \times 10 \times 125.7$ in $x \times y \times z$ and resolution $192 \times 65 \times 96$ Fourier, Chebyshev, Fourier modes respectively. The Reynolds number is $R = 337.9$ with $\ell = 10^2$ and the cross-flow velocity $W_\infty = 1.44232\,U_\infty(x = 0)$ and $m = 0.34207$. These particular kernels were computed, at high resolution, for the purpose of visualization and are not used in the simulations presented here. They are however representative for all the kernels used in terms of their shape and structure. Notice that the kernels show that the control mainly relies on upstream information, and that the convective time delay of the mean flow profiles is taken into account automatically. Turning and twisting the kernel one can see that it is skewed in a way corresponding to the direction of the mean-flow streamline varying with y. Another important property of the kernels is their spatial localization, which is crucial to allow extension to the spatially developing flow in § 2.4. As an alternative to the approach presented here, the problem could be formulated in the spatial setting directly. In Cathalifaud & Luchini (2000), the boundary layer equations are used in an adjoint-based optimization framework, and Joslin *et al.* (1997) consider a similar problem for the two-dimensional Navier–Stokes equations. A major difference between the present (Riccati-based) approach and the adjoint-based approach is that the latter does not yield constant gain feedback laws.

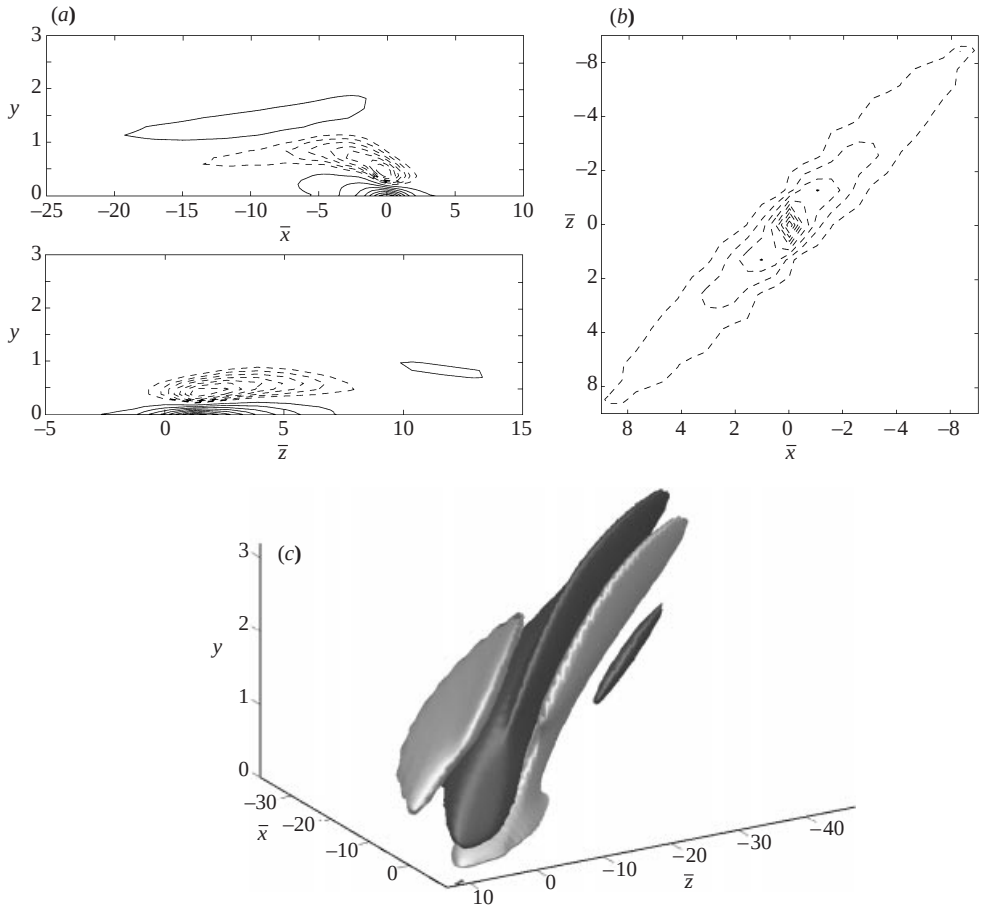

FIGURE 2. Control convolution kernel for the normal velocity computed at $R = 337.9$ with $\ell = 10^2$ and $r^2 = 0$ with a resolution of $192 \times 65 \times 96$ Fourier, Chebyshev, Fourier modes in an $x \times y \times z$ box with the dimensions $100 \times 10 \times 125.7$ respectively. (*a*) Contour plots of the (x, y)- and (z, y)-plane and $z = 0$ and $x = 0$ respectively. Solid contours are positive values and dashed contours are negative. (*b*) Contour plot of the (x, z)-plane at $y = 0$ (corresponding to k_φ in (2.30)). (*c*) Isosurfaces at 25 (light) and -25 (dark).

2.4. *Extension to spatially developing boundary layers*

The key property necessary for the controller to work for a spatially developing boundary layer is that it only utilizes local information about the flow and that non-parallel effects are small. Assuming that non-parallel effects are small is not valid for many flows since the growth of the boundary layer can have a substantial effect on the eigenvalues of the system. This can however be of less significance for the application of control since the precise eigenvalues are not as important as the overall dynamics. In the case with cross-flow there is also a change in the direction of the outer streamline in the chordwise direction that is not accounted for with the parallel assumption. Some robustness of the controller performance with respect to a varying mean flow is expected based on the success in relaminarizing a low Reynolds number turbulent channel flow in Högberg (2001). This indicates that the controller can handle finite deviations of the mean flow from that for which it was computed. The localization of the convolution kernels implies that only information on the flow field

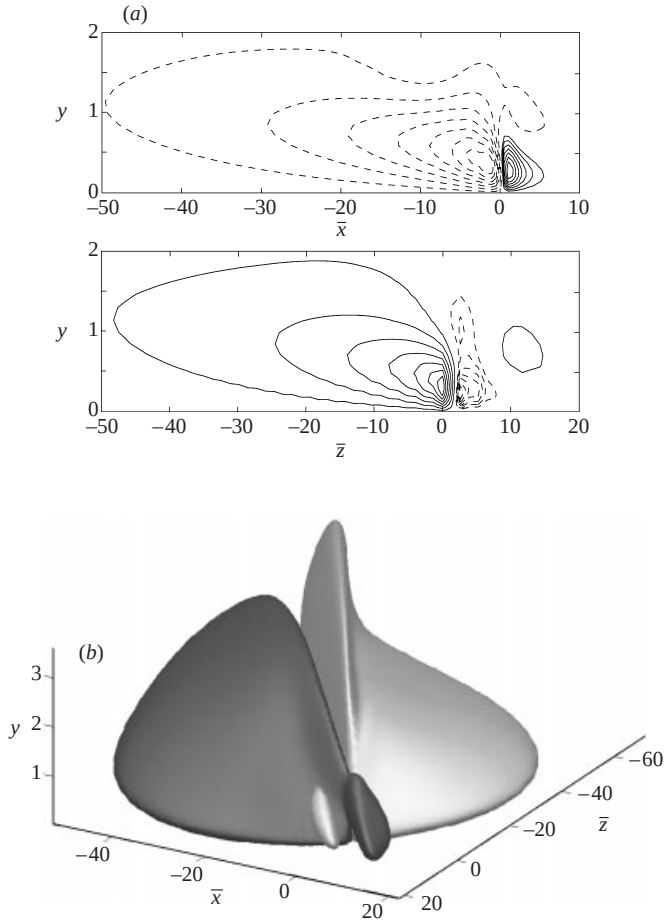

FIGURE 3. Control convolution kernel for the normal vorticity computed at $R = 337.9$ with $\ell = 10^2$ and $r^2 = 0$ with a resolution of $192 \times 65 \times 96$ Fourier, Chebyshev, Fourier modes in an $x \times y \times z$ box with the dimensions $100 \times 10 \times 125.7$ respectively. (a) Contour plots of the (x, y)- and (z, y)-plane at $z = 0$ and $x = 0$ respectively. Solid contours are positive values and dashed contours are negative. (b) Isosurfaces at 0.5 (light) and -0.5 (dark).

close to the actuation region is used. The property of spatial localization also extends from the channel to the boundary layer flows as demonstrated in figures 2 and 3.

The control kernel is computed in the spatial case in the same way as in the temporal case using a base flow profile at some position where the control will be centred. At every time step of the simulations, the convolution is computed for the entire domain. The time derivative of the normal velocity on the wall is then obtained and used to update the control used in the current time step. A filtering procedure is then applied to confine the control action to the specified interval and give the boundary condition for the next time step. To ensure zero mass flux after the filtering of the control a constant is added to the control,

$$\breve{\varphi}(x, z) = (\varphi(x, z) + c)H(x), \quad \text{where} \quad c = -\frac{\int_z \int_x \varphi(x, z)\, H(x)\, \mathrm{d}x\, \mathrm{d}z}{zl \int_x H(x)\, \mathrm{d}x}, \tag{2.31}$$

and $H(x)$ is a hat function consisting of a combination of two step functions. The step function is defined as

$$S(r) = \begin{cases} 0, & r \leqslant 0 \\ 1/\left[1 + \exp\left(\dfrac{1}{r-1} + \dfrac{1}{r}\right)\right], & 0 < r < 1 \\ 1, & r \geqslant 1, \end{cases} \tag{2.32}$$

where $r = (x - x_0)/\Delta x$ is used to allow the slope, position and the extent of the S function to be changed. Using the step function described by equation (2.32), the hat function is defined such that

$$H(x) = S\left(\frac{x - (x_c - x_l/2)}{\Delta x}\right) - S\left(\frac{x - (x_c + x_l/2)}{\Delta x}\right), \tag{2.33}$$

where x_c is the position where the control is computed, x_l is the length of the control interval and Δx is the rise and fall distance.

Since a spectral method is used for discretization we can compute the convolution integral as a sum in Fourier space. In the parallel flow only the $\alpha = \beta = 0$ mode contains the mean flow, but in a spatial simulation the mean flow varies in the chordwise direction and all Fourier modes with $\beta = 0$ are used to describe it. This means that in the perturbed flow, all modes with $\beta = 0$ contain two components, one from the mean flow and one from the perturbation. Since the controller is designed for feedback of the perturbation only, the mean flow component must be subtracted from the mode before the convolution is computed. One can expect that the controller will work as well as in the temporal case locally near the position where the mean flow corresponds to that for which the optimal controller was computed. Further away from this position the computed control is not expected to be as good.

3. Numerical issues

3.1. *Discretization and solution of control problem*

The equations are discretized in y using a Chebyshev collocation technique utilizing the Gauss–Lobatto collocation points such that

$$\underline{f} = [\underline{f}_1, \ldots, \underline{f}_N]^T, \quad \text{where} \quad y_j = \cos\left(\frac{(j-1)\pi}{N-1}\right), \quad j = 1, \ldots, N, \quad \underline{\mathbf{f}}_i \approx f(y_i).$$

The bar under a variable $\underline{(\,)}$ will be used to distinguish discrete variables and operators from their continuous counterparts. The operators are mapped to the Chebyshev interval $-1 \leqslant y \leqslant 1$ and then the discrete operators are compiled using the spectral MATLAB Differentiation Matrix Suite of Weideman & Reddy (2000). In particular this suite provides fourth-order differentiation matrices invoking clamped boundary conditions ($f(\pm 1) = f'(\pm 1) = 0$) that gives an Orr–Sommerfeld matrix with nice numerical properties avoiding spurious modes. Integration weights $\underline{\boldsymbol{W}}$ for the Chebyshev grid with the Gauss–Lobatto collocation points are computed using an algorithm described in the appendix of Hanifi, Schmid & Henningson (1996),

$$\int_{-1}^{1} f(y)\,\mathrm{d}y = \sum_{j=1}^{N} \underline{\mathbf{f}}_j \underline{\boldsymbol{W}}(y_j), \quad \underline{\boldsymbol{W}}(y_j) = \frac{b_j}{N} \sum_{n=0}^{N-1} c_n \cos\left(\frac{n\,j\,\pi}{N-1}\right) \int_{-1}^{1} T_n(y) \frac{\mathrm{d}y'}{\mathrm{d}y}\,\mathrm{d}y,$$

where y' is the physical normal coordinate in the boundary layer mapped to the Chebyshev interval $-1 \leqslant y \leqslant 1$ and $\{T_n(y)\}_{n=0}^{N-1}$ are the Chebyshev polynomials. The

coefficients b_j and c_n are found from

$$f(y) = \sum_{n=0}^{N-1} \tilde{f}_n T_n(y) = \sum_{n=0}^{N-1} c_n T_n(y) \sum_{j=1}^{N} \frac{b_j}{N} f(y_j)\, T_n(y_j),$$

where $\tilde{f}_n$ denotes the coefficients obtained from a Chebyshev transform of f. These weights provide spectral accuracy of the integration. We can then introduce the diagonal matrix $\underline{\boldsymbol{\Theta}}$ such that

$$\underline{\boldsymbol{\Theta}}_{ij} = \delta_{ij} \underline{W}(y_j),$$

where δ_{ij} is the Kronecker delta. The matrix $\underline{\boldsymbol{\Theta}}$ can be viewed as the 'mass' matrix for the Chebyshev grid. The inner product for the discrete system, approximating the one used in the continuous case, is then such that

$$\langle f, g \rangle \approx \int_0^\infty \underline{f}^* \underline{\boldsymbol{\Theta}} \underline{g}\, \mathrm{d}t.$$

The mass matrix is also used in the compilation of the discrete form of the energy measure operator $\mathscr{Q}$ in (2.20) such that the discrete objective function is

$$\underline{J} = \int_0^\infty \hat{\underline{x}}^* \underline{\boldsymbol{Q}} \hat{\underline{x}} + \ell^2 \hat{\underline{\phi}}^* \hat{\underline{\phi}}\, \mathrm{d}t,$$

and the discrete adjoint equation and the discrete feedback law are

$$-\dot{\hat{\underline{p}}} = \underline{\boldsymbol{A}}^* \hat{\underline{p}} + \underline{\boldsymbol{Q}} \hat{\underline{x}}, \quad \hat{\underline{p}}(t \to \infty) = 0, \quad \hat{\underline{\phi}} = -\frac{1}{\ell^2} \underline{\boldsymbol{B}}^* \hat{\underline{p}}.$$

Once everything is expressed in discrete form, an algorithm taken from Skelton (1988, p. 350) and implemented in MATLAB is used to solve the discrete version of the Riccati equation (2.25). The heart of this computation is the eigenvalue problem obtained by combining the state and adjoint equations,

$$\frac{\mathrm{d}}{\mathrm{d}t} \begin{bmatrix} \hat{\underline{x}} \\ \hat{\underline{p}} \end{bmatrix} = \begin{bmatrix} \underline{\boldsymbol{A}} & -(1/\ell^2)\underline{\boldsymbol{B}}^* \underline{\boldsymbol{B}} \\ -\underline{\boldsymbol{Q}} & -\underline{\boldsymbol{A}}^* \end{bmatrix} \begin{bmatrix} \hat{\underline{x}} \\ \hat{\underline{p}} \end{bmatrix} \Rightarrow \begin{bmatrix} \underline{\boldsymbol{A}} & -(1/\ell^2)\underline{\boldsymbol{B}}^* \underline{\boldsymbol{B}} \\ -\underline{\boldsymbol{Q}} & -\underline{\boldsymbol{A}}^* \end{bmatrix} \begin{bmatrix} \underline{\boldsymbol{E}}_1 \\ \underline{\boldsymbol{E}}_2 \end{bmatrix} = \underline{\boldsymbol{\Lambda}} \begin{bmatrix} \underline{\boldsymbol{E}}_1 \\ \underline{\boldsymbol{E}}_2 \end{bmatrix}.$$

When the array of eigenvectors $[\underline{\boldsymbol{E}}_1, \underline{\boldsymbol{E}}_2]^T$ and the matrix of eigenvalues $\underline{\boldsymbol{\Lambda}}$ are available, they are sorted in increasing order so that both the state equation and the adjoint equation are stable. The solution of the discrete Riccati equation, if it exists, is then given from this sorted solution to the eigenvalue problem as

$$\underline{\boldsymbol{E}}_2 = \hat{\underline{\boldsymbol{X}}} \underline{\boldsymbol{E}}_1 \Rightarrow \hat{\underline{\boldsymbol{X}}} = \underline{\boldsymbol{E}}_2 \underline{\boldsymbol{E}}_1^{-1},$$

since $\hat{\underline{\boldsymbol{X}}}$ is the linear mapping from $\hat{\underline{x}}$ to $\hat{\underline{p}}$ introduced in the same way as in the derivation of the Riccati equation in § 2.3. For a detailed study of Riccati equations and methods to find their solutions see e.g. Laub (1991) or Hulsing (1999). Now the discrete version of the feedback operator is given by

$$\hat{\underline{\boldsymbol{K}}} = -\frac{1}{\ell^2} \underline{\boldsymbol{B}}^* \hat{\underline{\boldsymbol{X}}}.$$

The inverse of $\underline{\boldsymbol{\Theta}}$ is then used to obtain the approximation of the integral kernel $\hat{\boldsymbol{k}}$ from the discrete form of $\hat{\boldsymbol{K}}$ in expression (2.29) such that

$$\hat{\underline{k}} = [\underline{\boldsymbol{\Theta}}^{-1} \hat{\underline{\boldsymbol{K}}}_{\hat{\underline{\xi}}}, \underline{\boldsymbol{\Theta}}^{-1} \hat{\underline{\boldsymbol{K}}}_{\hat{\underline{\eta}}}, \hat{\mathscr{K}}_{\hat{\underline{\phi}}}].$$

By specifying the size and resolution of a periodic domain in x and z, an array of wavenumber pairs (α_i, β_j) is implicitly given. By computing $\hat{\underline{\boldsymbol{k}}}\ (\alpha_i, \underline{y}, \beta_j)$ for all wavenumber pairs, a discrete Fourier representation approximating the continuous feedback kernel is obtained. Through a two-dimensional inverse FFT of the array of controllers, we then obtain the physical-space convolution kernels like those exemplified in figures 2 and 3. It is shown in Högberg (2001) that the kernels computed through the present approach are independent of the box size if the periodic domain is sufficiently large.

3.2. *Direct numerical simulations*

A spectral method is used to solve the incompressible Navier–Stokes equations for flow over a flat plate with a pressure gradient. The equation solved is

$$\left.\begin{aligned} \frac{\partial \boldsymbol{u}}{\partial t} &= NS(\boldsymbol{u}) + \lambda(x)(\boldsymbol{u} - \boldsymbol{u}_\lambda) + \boldsymbol{F}, \\ \nabla \cdot \boldsymbol{u} &= 0, \end{aligned}\right\} \tag{3.1}$$

where NS represents the Navier–Stokes equations. To retain the periodic boundary conditions and allow a streamwise inflow and outflow to and from the computational domain, a fringe region technique (see e.g. Nordin & Henningson 1999) is used in the spatial simulations. This is implemented in the term $\lambda(x)(\boldsymbol{u} - \boldsymbol{u}_\lambda)$, where $\lambda(x)$ is a positive function that is non-zero only at the end of the computational domain and $\boldsymbol{u}_\lambda$ is the desired solution in this region. The term $\boldsymbol{F} = [F_1, F_2, F_3]^T$ represents additional forcing used to introduce perturbations in the flow in spatial simulations or to maintain a particular mean flow in the temporal simulations. An artificial boundary is introduced and a free-stream boundary condition applied at a constant distance from the flat plate. The normal direction is discretized using Chebyshev polynomials and the horizontal directions by Fourier series with dealiasing according to the 3/2-rule. Time integration is performed using a third-order Runge–Kutta method for the advective and forcing terms and a Crank–Nicholson method for the viscous terms. Other articles where descriptions of this code are available are e.g. Högberg & Henningson (1998) and Berlin, Wiegel & Henningson (1999). All the details of the code can be found in Lundbladh *et al.* (1999).

3.2.1. *Temporal simulations*

In the temporal (parallel) case we have $\lambda(x) = 0$ and a forcing of the form

$$\boldsymbol{F} = \left[-\frac{1}{R}\frac{\partial^2 U(y)}{\partial y^2}, 0, -\frac{1}{R}\frac{W_\infty}{U_\infty}\frac{\partial^2 W(y)}{\partial y^2} \right]^T$$

is used to maintain a constant parallel flow in time in the entire computational domain. The mean velocities $U(y)$ and $W(y)$ are given for a specified position x_0 by (2.6) and 2.7 respectively. The boundary condition employed at the upper boundary is $\mathrm{D}u' = \mathrm{D}v' = \mathrm{D}w' = 0$ and a perturbation is introduced through the initial velocity fields where an eigenvector, computed for a particular wavenumber pair and scaled to a given perturbation energy, provides the velocity distribution. This initial velocity field is then marched in time to ensure that no transients are present in the flow and that the correct growth rate is obtained. Control is then computed and applied through blowing and suction along the entire wall in the temporal simulations. The parameters used in the temporal simulations presented in this paper are given for cases 1–4 in table 1.

Case	Flow	Perturbation	Control		
			r^2	ℓ	$x \in$
1	A	Eigenmode		none	
2	A	Eigenmode	0	10^5	all
3	A	Eigenmode	10^5	10^5	all
4	A	Eigenmode	0	10^2	all
5	B	TS wave		none	
6	B	TS wave	0	10^2	[75, 225]
7	B	Optimal		none	
8	B	Optimal	0	10^2	[75, 225]
9	B	Optimal	0	10^2	[75, 725]
10	C	Random		none	
11	C	Random	0	10^2	[75, 225]
12	D	Stationary		none	
13	E	Stationary	0	10^2	[25, 175]
14	E	Stationary	0	10^2	[145, 295]

Letter	Flow	Resolution	Box	Fringe				
				x_{start}	x_{mix}	Δ_{mix}	Δ_{rise}	Δ_{fall}
A	Temporal FSC	$4 \times 49 \times 4$	$25.14 \times 10 \times 25.14$	none				
B	Spatial Blasius	$576 \times 65 \times 4$	$1128 \times 20 \times 12.83$	1028	1028	40	100	20
C	Spatial FSC	$192 \times 49 \times 48$	$500 \times 8 \times 251.4$	350	400	40	100	20
D	Spatial FSC	$576 \times 65 \times 24$	$500 \times 8 \times 25.14$	350	400	40	100	20
E	Spatial FSC	$384 \times 49 \times 16$	$500 \times 8 \times 25.14$	350	400	40	100	20

TABLE 1. Overview of simulations performed. The control kernels are always computed using velocity profiles from the centre of the control interval and at the same box size and resolution as the simulation. The rise and fall scale of the control region is $\Delta x = 5$ in all cases. The Reynolds number is $R = 337.9$ for the FSC cases and $R = 468.34$ for the Blasius cases. The fringe region in the spatial simulations always ends at the end of the box and $\lambda_{max} = 0.4$ in all cases.

3.2.2. *Spatial simulations*

For spatial simulation the fringe forcing term is used to make the solution to (3.1) periodic. This enables us to use spectral methods for simulation of the spatial flow also even though a part of the domain (the fringe region) will be non-physical. The fringe forcing with the maximum value λ_{max} is compiled using the step function (2.32) and has the form

$$\lambda(x) = \lambda_{max}\left[S\left(\frac{x - x_{start}}{\Delta_{rise}}\right) - S\left(\frac{x - x_{end}}{\Delta_{fall}} + 1\right)\right], \tag{3.2}$$

where x_{start} and x_{end} are the start and end of the fringe region and Δ_{rise} and Δ_{fall} are the rise and fall distance of the fringe forcing respectively. An initial guess for the velocity field is first obtained from (2.6) and (2.7) such that $U = U(x, y)$, $W = W(x, y)$. A smooth blending in the fringe region is used to make the flow periodic and we obtain

$$\boldsymbol{u}_\lambda = [u_\lambda, v_\lambda, w_\lambda]^T,$$

where

$$u_\lambda = U(x, y) + \left[U(x - x_L, y) - U(x, y) + u_p(x - x_L, y, t)\right] S\left(\frac{x - x_{mix}}{\Delta_{mix}}\right),$$

$$w_\lambda = W(x, y) + \left[W(x - x_L, y) - W(x, y) + w_p(x - x_L, y, t)\right] S\left(\frac{x - x_{mix}}{\Delta_{mix}}\right),$$

where x_L is the period of the domain in x. The coordinate x_{mix} and the parameter Δ_{mix} denote the start of the blending region and its rise distance respectively. The normal velocity v_λ is then computed from continuity. This gives the flow field used to compute the boundary conditions as well as the desired flow in the fringe forcing term. The free-stream boundary condition used in the spatial simulations is $\mathrm{D}u' + ku' = \mathrm{D}u_\lambda + ku_\lambda$, $\mathrm{D}v' + kv' = \mathrm{D}v_\lambda + kv_\lambda$ and $\mathrm{D}w' + kw' = \mathrm{D}w_\lambda + kw_\lambda$, where k is the modulus of the horizontal wavenumber ($k^2 = \alpha^2 + \beta^2$). The initial velocity field is then relaxed to a stationary solution of the Navier–Stokes equations by running a simulation without perturbations for a sufficiently long time. The velocity field obtained through this procedure is then used as the initial condition in the spatial simulations with perturbations and control.

The disturbances in the flow field can be generated either by forcing to a particular perturbation in the fringe region or by applying an external volume force somewhere in the computational domain. The forcing used to generate perturbations in the fringe is introduced through $\boldsymbol{u}_\lambda$ using $u_p(x, y, t)$ and $w_p(x, y, t)$. In the present simulations this forcing has been used to introduce the optimal perturbation in the Blasius boundary layer for cases 7–9 in table 1 where u_p and w_p were computed from the boundary layer equations as in Andersson, Berggren & Henningson (1999).

Both stationary and time-varying perturbations can be generated through an external volume force. A random forcing is constructed by randomly distributing the amplitude among a given number of spanwise Fourier components at each time interval. This forcing, which is directed normal to the wall, has the form

$$F_2 = F_{\mathrm{rand}} = \exp(-((x - x_0)/x_{\mathrm{scale}})^2 - (y/y_{\mathrm{scale}})^2)\, f(z, t), \tag{3.3}$$

where

$$f(z, t) = \mathrm{amp}_t[(1 - b(t))\, h^i(z) + b(t)\, h^{i+1}(z)] \tag{3.4}$$

and

$$i = \mathrm{int}(t/t_{\mathrm{d}t}), \tag{3.5}$$

$$b(t) = 3p^2 - 2p^3, \tag{3.6}$$

$$p = t/t_{\mathrm{d}t} - i, \tag{3.7}$$

where $g(z)$ and $h^i(z)$ are Fourier series of unit amplitude with random coefficients, and amp_t is the amplitude. The number of random coefficients in each Fourier series is given by a parameter named n_{modes}. Random values are generated for $h^i(z)$ with the spacing $t_{\mathrm{d}t}$ in time and then the ramp function $b(t)$ is used to interpolate this to a smooth forcing. This forcing is used to generate the travelling cross-flow vortices for cases 10–11 in table 1 and the parameter values for the forcing are given in table 2.

The harmonic disturbance is constructed as an exponentially decaying function centred at $y = 0$ and $x = x_0$. It is also possible to give a relationship between the x- and z-components of the disturbance to align the disturbance to a streamline. The harmonic forcing has the form

$$F_2 = F_{\mathrm{harm}} = \mathrm{amp}_s \exp(-(y/y_{\mathrm{scale}})^2)\, g(x, z)\, h_1(t), \tag{3.8}$$

where

$$g(x, z) = \begin{cases} \cos(2\pi(z - x\, l_{\mathrm{skew}})/z_{\mathrm{scale}}) \exp(-[(x - x_0)/x_{\mathrm{scale}}]^2) & \text{if} \quad z_{\mathrm{scale}} \neq 0, \\ \exp(-[(x - x_0)/x_{\mathrm{scale}}]^2) & \text{if} \quad z_{\mathrm{scale}} = 0, \end{cases} \tag{3.9}$$

	Cases		
Parameter	5–6	10–11	12–14
x_0	20	20.59	20.59
amp_t		0.001	
amp_s	0.0001		0.0036
x_{scale}	5	10	10
y_{scale}	1	1	1
z_{scale}	0		−25.14
l_{skew}			1
n_{modes}		21	
t_{dt}		1	
ω_h	0.093668		0

TABLE 2. Forcing parameters for the spatial simulations of cases 5–14.

where

$$h_1(t) = \cos(\omega_h t). \tag{3.10}$$

For stationary disturbances ω_h is chosen as zero, otherwise it is the ω value of the particular perturbation. In the simulations presented in this paper the amplitude is given by amp_s for stationary disturbances or amp_t for time-dependent (oscillating) disturbances. The Tollmien–Schlichting wave in cases 5 and 6 is generated using this harmonic forcing with the parameters given in table 2. An oblique stationary forcing is used to generate the stationary cross-flow vortices for cases 12–14 in table 1 with the parameters given in table 2. The other parameters concerning e.g. box sizes and fringe regions used in the spatial simulations presented in this paper are given for cases 5–14 in table 1.

4. Control in a parallel boundary layer

In order to examine the properties of the computed control, the parallel boundary layer flow is studied. This simple case allows us to illustrate and verify the effect of the control and the parameters of the objective function in terms of temporal eigenvalues and eigenvectors. It also serves as a tool to validate the numerical implementation of the control algorithm. In a boundary layer flow with a three-dimensional velocity profile one can always find a direction in which an inviscid instability can exist due to inflection points in the velocity profile. In this direction there will be an unstable eigenvalue with a corresponding eigenmode. We will focus on the flow investigated in Högberg & Henningson (1998) where the Reynolds number was $R = 337.9$ at the beginning of the simulation box with a cross-flow velocity $W_\infty = 1.44232 U_\infty(x = 0)$, $m = 0.34207$ and the width of the box was $z_l = 25.14$. This flow was studied in spatial simulations and in § 6 the control will be applied to a few of those cases.

A study of the effect on eigenvalues and eigenvectors of the control is shown in figure 4. The uncontrolled eigenvalues are those of $\boldsymbol{N}$ in (2.14) shown with the open circles in figure 4(*a*), and the controlled eigenvalues are those of the closed loop system $\boldsymbol{A}_{cl}$ in (2.26). The unstable eigenvalue $(-0.15246 + \text{i}0.0382)$ is moved by a controller with $\ell = 10^5$ and $r = 0$ to $(-0.15246 - \text{i}0.0382)$, where the closed loop eigenvalues are plotted as crosses in figure 4(*a*). The corresponding

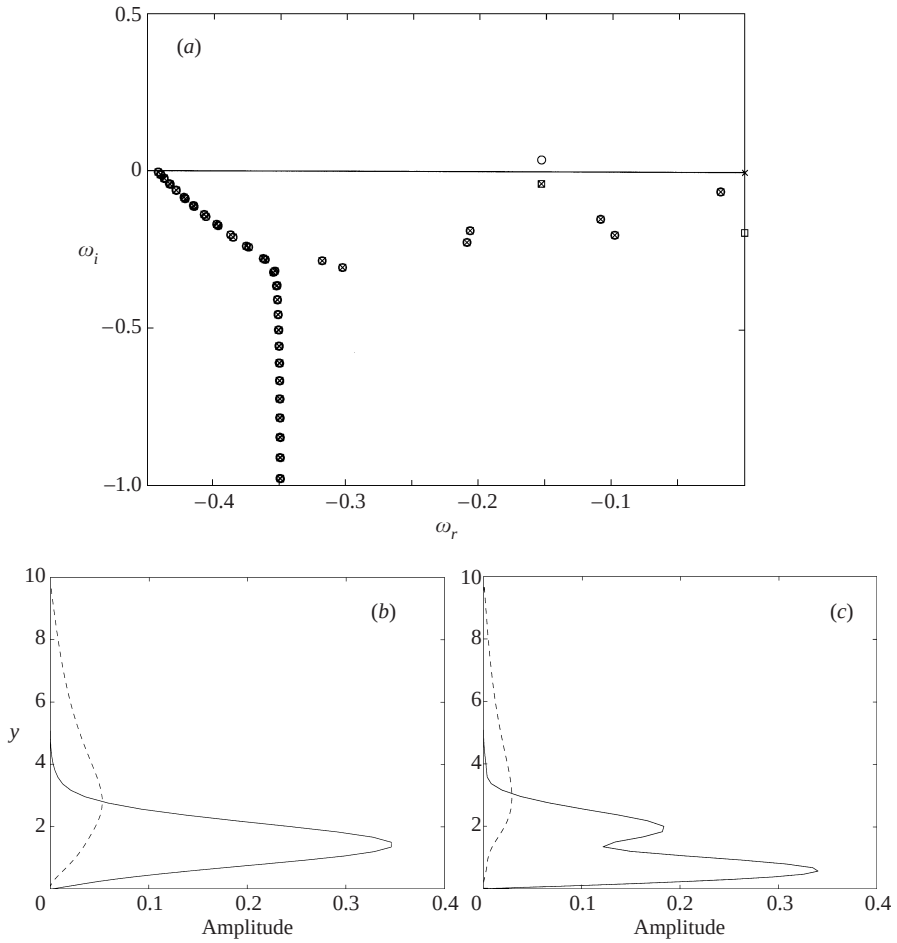

FIGURE 4. Effect of control on unstable eigenvalues and corresponding eigenvectors. The parameters are $\alpha = 0.25$, $\beta = -0.25$ with 90 collocation points in y. Uncontrolled eigenvalues and eigenvectors are for $\boldsymbol{N}$ from (2.14) and controlled ones are for the closed loop system $\boldsymbol{A}_{cl}$ in (2.26). (*a*) The uncontrolled eigenvalues are represented by ○, the controlled ones by x for $\ell = 10^5$, $r = 0$ and by □ for $\ell = 10^5$, $r^2 = 10^5$. (*b*) The absolute value of the uncontrolled unstable eigenvector, solid curve is η and dashed v. (*c*) The absolute value of the corresponding controlled eigenvector with $\ell = 10^5$, solid curve is η and dashed v. This eigenvector is identical for both values of r^2.

eigenvector also is modified by the control, compare figures 4(*b*) and 4(*c*). The high penalty on the control parameter results in only the unstable eigenvalue being moved. In fact, it is just reflected in the real axis. The reflection of the unstable eigenmode in the real axis obtained through application of control with extremely large penalty (ℓ) is because this is the cheapest way for the controller to stabilize the system in terms of control effort. Bewely & Liu (1998) referred to this as the 'expensive control' limit, meaning that no matter how high the penalty on the control is, the minimum requirement on the controller is that it at least stabilizes the system. An additional eigenvalue appears with the value $0.000001 - i0.000602$ and is due to the extra degree of freedom introduced to apply the control, and is now the most unstable eigenvalue in the controlled system. The position of this eigenvalue is expected since it corresponds to a mode with a slow variation in time and

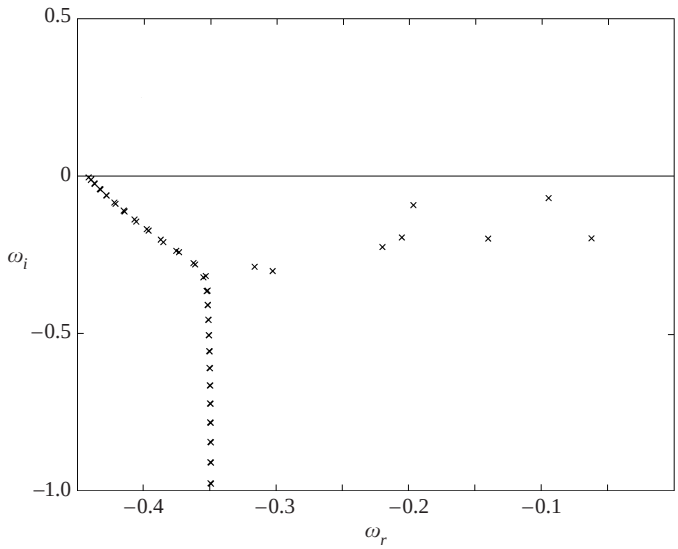

FIGURE 5. Controlled eigenvalues of $\boldsymbol{A}_{cl}$ in (2.26) for a controller with $\ell = 10^2$, $r = 0$.

thereby a low cost in the objective function. Using the extra penalty term (r^2) on φ^2 in the objective function will move this eigenvalue down the imaginary axis since in this case also the stationary value will be expensive. With $r^2 = 10^5$ this eigenvalue will move to $(10^{-8} - \mathrm{i}0.190367)$, shown with the closed loop eigenvalues denoted by an open square in figure 4(a). With a lower penalty ℓ the unstable eigenvalue would move more and other eigenvalues would also be moved in order to obtain exactly the system dynamics that minimizes the objective function, as illustrated in figure 5. The movement of eigenvalues and modifications of eigenvectors through application of control is discussed in Bewley & Liu (1998) in terms of channel flow. They show that the application of the control makes the eigenvectors 'more orthogonal' and thereby lowers the transient energy growth. Joshi *et al.* (1997) also study the effect of controllers on eigenvalues for channel flow.

In temporal direct numerical simulations the eigenvector in figure 4(b) is used as initial perturbation with an energy density of 2×10^{-11}. Then feedback control is applied first with $\ell = 10^5$, $r^2 = 0$ and then with $\ell = 10^5$, $r^2 = 10^5$ and finally with $\ell = 10^2$, $r^2 = 0$. In figure 6 the energy growth for these different simulations for cases 1–4 in table 1 is shown. The decay of the perturbation after control has been applied is different for the different values of the penalty parameters ℓ and r. The slope in the cases where $\ell = 10^5$ and the uncontrolled case corresponds to the largest eigenvalue of the dynamical system. In summary the application of the linear control strategy to parallel boundary layers gives results analogous to those obtained for channel flow in previous studies.

5. Control in a Blasius boundary layer

To test the strategy on a simple case the Blasius boundary layer is studied for one case with a TS wave and one case with the optimal perturbation for spatial transient growth. The Blasius mean flow profile is a special case of the Falkner–Skan profiles with $m = 0$ and no mean-flow component in the z-direction. A TS wave is generated

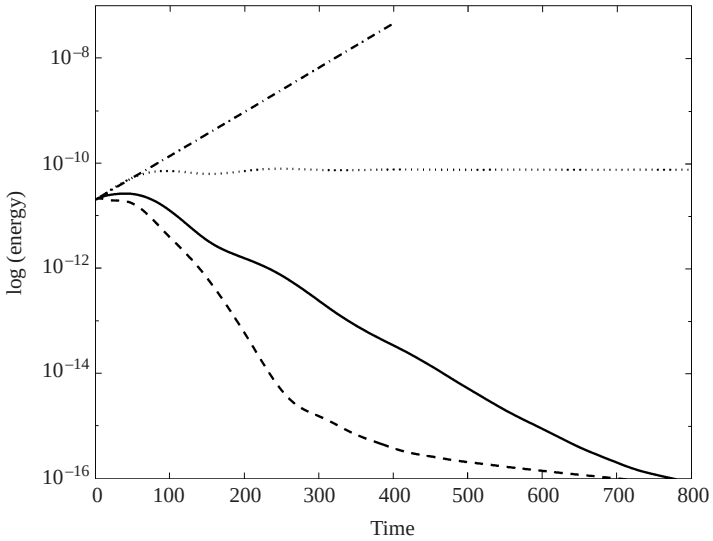

FIGURE 6. Energy growth of an uncontrolled unstable eigenvector perturbation and the effect of applied controls. Dash-dot: uncontrolled energy growth from case 1, dotted: controlled with $\ell = 10^5$ and $r^2 = 0$ from case 2, solid: controlled with $\ell = 10^5$ and $r^2 = 10^5$ from case 3, dashed: controlled with $\ell = 10^2$ and $r^2 = 0$ from case 4.

by an oscillating two-dimensional forcing at the dimensionless frequency $F = 200$, where $F = 2\pi f \nu / U_\infty^2 \times 10^6$, at the beginning of the box and allowed to develop downstream. The domain and resolution for the simulation is given in table 1, case 5. The flow is perturbed just upstream of branch I of the neutral stability curve which is at about $Re = 507$ and the perturbation grows exponentially, shown as the dashed line in figure 7(a), in the uncontrolled case until it reaches branch II at about $Re = 723$. The small transient at the beginning is because we do not force to a pure TS eigenmode. In case 6 in table 1 the controller applied between $Re = 568.4$ and $Re = 729$ corresponding to $x \in [75, 225]$. The solid line in figure 7(a) shows that the exponential growth is completely removed by the controller in the control region and instead there is exponential decay. These results are similar to those obtained by Walther *et al.* (2001) where the application of control resulted in exponential decay of the perturbation energy in the unstable region. In figure 7(b) the control signal on the wall is plotted at different times during a period of the TS wave. The control signal looks like a wave with decaying amplitude and is periodic in time.

Next the performance of the controller for a transiently growing perturbation is studied. The spatial optimal perturbations in a Blasius boundary layer have been computed by Andersson *et al.* (1999) and Luchini (2000). The particular optimal spatial perturbation used here is computed using the technique from Andersson *et al.* (1999); it is introduced at $x = -158.16$ where the local Reynolds number is $R_0 = 395.4$ and then marched forward using the linear equations to the position where $x = 0$ where the simulation box starts and the local Reynolds number is $Re = 468.34$. The perturbation is optimized to be the one with maximum growth at $x = 237.24$ in the simulation box. Notice that this means that no other perturbation can cause larger growth at this particular position, which does not necessarily imply that the perturbation has its maximum at this position unless it is the global optimal perturbation. This perturbation is then used in DNS with and without control. The domain and resolution are given in table 1 for case 7 which is the uncontrolled

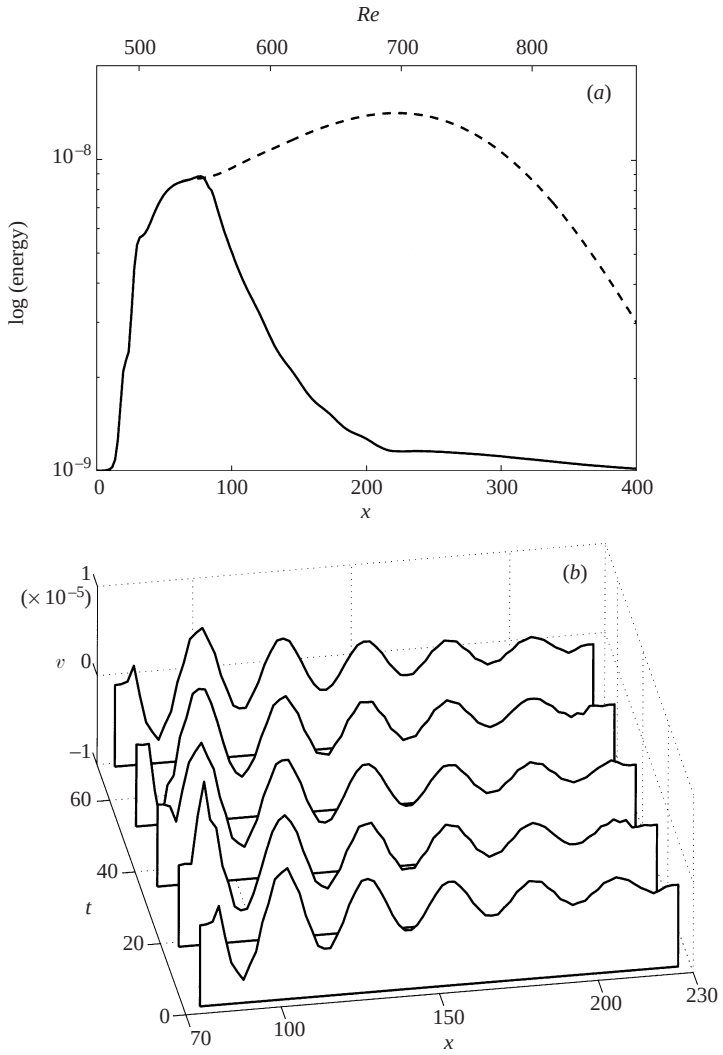

FIGURE 7. (*a*) The spatial energy growth of a TS wave perturbation in a Blasius boundary layer with control from case 6 (solid) and without control from case 5 (dashed). The non-dimensional frequency of the perturbation is $F = 200$. Control is applied in $x \in [75, 225]$. (*b*) Control signal during one time period of the TS wave.

flow. In figure 8(*a*) the dotted line shows the energy evolution as the perturbation is marched using the linear equations. The solid line shows the result for the uncontrolled perturbation using DNS. The energy measure is defined as

$$E(\boldsymbol{u}(x)) = \int_0^{2\pi/\beta} \int_0^{\infty} (u^2 + v^2 + w^2)\,\mathrm{d}y\,\mathrm{d}z,$$

and E_0 is the energy of the perturbation at the initial position.

In case 8 the same controller and control interval as in the TS wave case (case 6) is used. In figure 8(*a*) the dash-dotted line shows the perturbation energy for this case. Here the simulation is run until a stationary state has been obtained. Immediately the perturbation reaches the control interval its energy is reduced and then continues

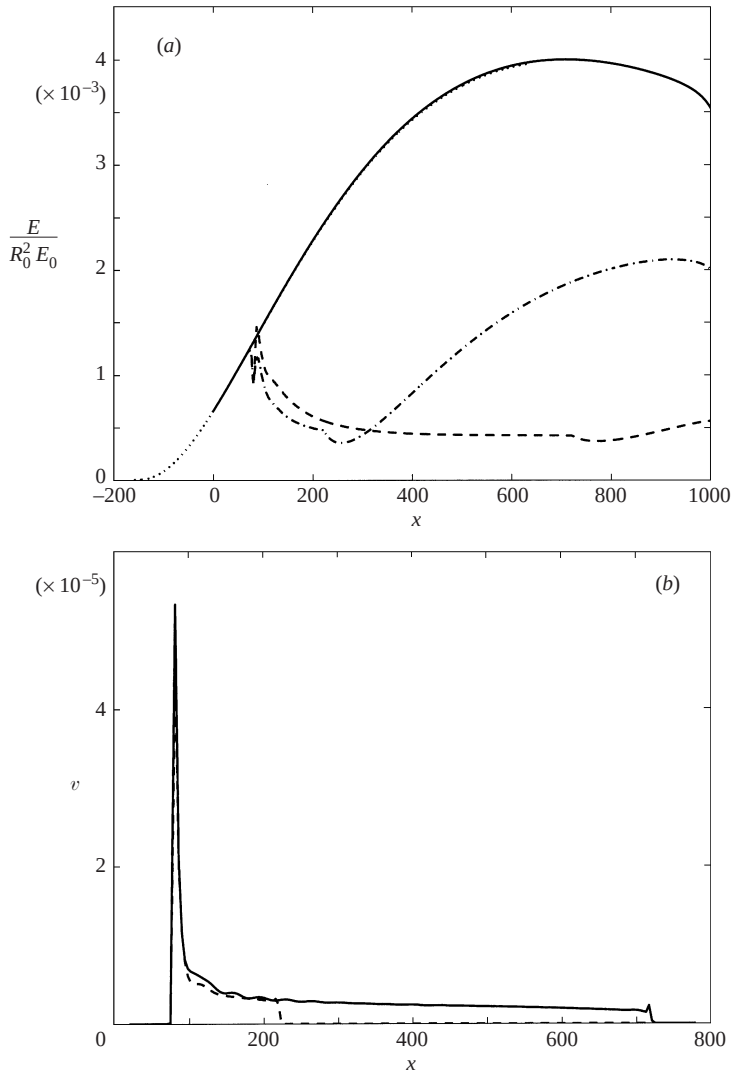

FIGURE 8. (*a*) The spatial energy growth of the optimal spatial perturbation at $x = 237.24$ with $R = 468.34$ in the Blasius boundary layer. Dotted: computed from the boundary layer equations. Solid: computed with DNS for case 7. Dash-dotted: with control applied in $x \in [75, 225]$ from case 8. Dashed: with control applied in $x \in [75, 725]$ from case 9. (*b*) The control (v) distribution at $y = z = 0$ for the streak mode in case 8 with control in $x \in [75, 725]$ (solid), and case 9 with control in $x \in [75, 225]$ (dashed).

to decay throughout the control interval. The control velocity for this case is plotted as the dashed line in figure 8(*b*) showing an initial peak and then a slowly decaying amplitude. Downstream of the control interval the perturbation grows again, but does not reach the same energy level as in the uncontrolled case.

In case 9 a controller computed further downstream, still with $l = 10^2$ and $r^2 = 0$, is applied in a longer region centred at $x = 400$ and for $x \in [75, 725]$. There is substantial growth of the boundary layer in this longer interval and the parallel assumption is truly challenged. Even though there is a larger difference in this case between the mean flow used to compute the control kernel and that at the position where the

control interval starts, the dashed line in figure 8(a) shows that the energy decays rapidly and is maintained at a low level by the control throughout the control interval. The control signal, solid line in figure 8(b), is similar to the one obtained for the shorter interval initially and then there is a slow decay in amplitude for the long interval case.

Comparisons with some of the results of Cathalifaud & Luchini (2000) where optimization is performed to minimize the perturbation energy with control over the whole plate show that the control velocity has a similar distribution and that a similar effect on the perturbation energy is obtained. In the cases where they apply control over only a small part of the plate, they found a slightly different shape of the control velocity distribution, with a peak also at the end of the interval. This is probably due to the optimization problem being slightly different in their case, accounting for the effects of the localization of the control, which is not the case for the optimization problem solved here.

The performance of the control over the longer control interval in case 9 is surprisingly good considering that the change of the mean flow profile is fairly large in this interval. It seems that the controller is indeed robust to finite variations of the mean flow profile and our assumption thereby appears justified.

6. Control in a Falkner–Skan–Cooke flow

6.1. *Travelling vortices*

The flows cases for testing the controller in the FSC flow are taken directly from Högberg & Henningson (1998). Travelling cross-flow vortices appear in experiments with high levels of free-stream turbulence, for example in Müller & Bippes (1988), and in the simulation of case 10 a perturbation, randomly varying in time and in space, is applied in the beginning of the box. A low amplitude ensures that nonlinear effects are small and travelling cross-flow vortices then develop downstream. The box size, resolution and other details are given in table 1. The time average of the perturbation energy, plotted as the dashed line in figure 9, shows the growth of these travelling vortices. The vortices merge and split and form a complicated pattern. A grey-scale image of a snapshot of the normal velocity at $y = 0.5$ is shown in figure 10(a) where whiter shades indicate positive velocity and darker shades negative velocity. In this case the control will have to react quickly in order to respond to the variation in the perturbation.

Control kernels have been computed at the same resolution and box size as in cases 10 and 11 in table 1, with $\ell = 10^2$ and $r^2 = 0$ at $x = 150$ where $\psi = 51.96^\circ$ and $\delta^* = 1.1232$. The control is then allowed to act in the interval $x \in [75, 225]$. The simulation is run long enough to obtain stationary statistics of the controlled flow and the time average of the energy in the box with control is plotted as the solid line in figure 9. The controller successfully changes the growth into decay of the energy and downstream of the control region there is again exponential growth of the perturbation all the way to the start of the fringe. The difference between the controlled and uncontrolled perturbation energy where the fringe region starts is about four decades. A snapshot of the normal velocity in case 11 is shown in figure 10(b) at the same y-plane and time as in the uncontrolled case. The apparent 'strip' in the beginning control interval clearly shows that the control action is strongest in the beginning of the control region, and since the vortices almost completely disappear after this the controller does not have to act so strongly downstream. Looking closely at figure 10(b) one can see that a light shade, indicating a positive normal velocity, leads to a dark spot

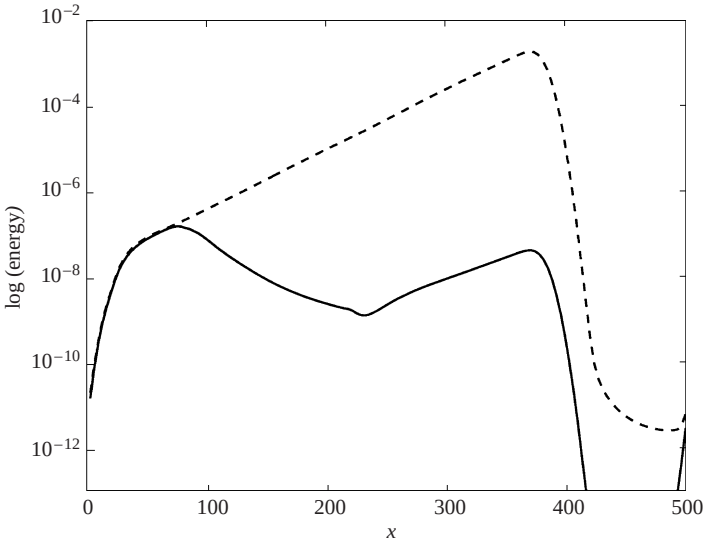

FIGURE 9. Time average of energy integrated in the z-direction for uncontrolled (dashed) and controlled (solid) simulations of travelling cross-flow vortices from cases 10 and 11 respectively.

in the control region, and vice versa for darker shades, suggesting that the control is of opposition type initially. In Wassermann & Kloker (2000) an opposition type control using blowing and suction in a strip where the optimal phase shift of the control signal was computed for each spanwise mode separately was applied to a cross-flow vortex packet. This strategy was also successful in reducing the perturbation energy, and the importance of the individually computed phase shift for different modes was emphasized. Using the present control strategy the optimal phase shift appears naturally which is a great advantage.

6.2. *Stationary vortices*

If stationary perturbations are introduced at the beginning of the box at a large enough amplitude, stationary nonlinearly saturated cross-flow vortices will develop downstream. The instability properties of these vortices have recently been thoroughly studied both experimentally by e.g. Kawakami, Kohama & Okutsu (1999) and Lerche (1997), and numerically by e.g. Högberg & Henningson (1998) and Malik *et al.* (1999). If we consider stationary perturbations at a finite amplitude applied at the beginning of the box in case 12 (box size and resolution is given in table 1), the vortices will reach a saturated level where nonlinearities dominate at the end of the physical region of the box. The energy in the $\beta = 0.25$ mode, the dashed line in figure 11, grows exponentially initially and then the nonlinear saturation causes the growth rate to decrease and close to the fringe the growth is close to zero. The energy of the five lowest beta modes is shown in figure 12(a) where one can see that all these modes have similar behaviour but the $\beta = 0.25$ mode dominates. Control is first applied in case 13 far enough upstream for linear effects to dominate. Kernels have been computed for the mean flow at $x = 100$ where $\psi = 52.95^\circ$ and $\delta^* = 1.085$ with $\ell = 10^2$, $r^2 = 0$ and with the box size and resolution given in table 1 for case 12. The simulations of the controlled flow are performed at a lower resolution than in the uncontrolled case with $384 \times 49 \times 16$ and use kernels with the same resolution. The control is allowed to act in the interval $x \in [25, 175]$ which starts just down-

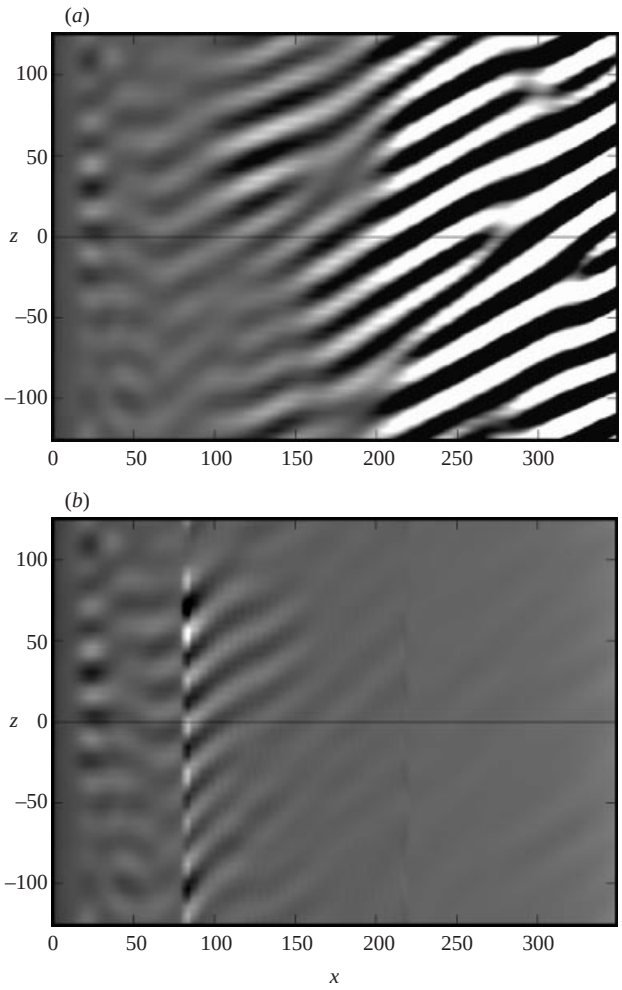

FIGURE 10. Snapshots of the normal velocity v in an (x, z)-plane at $y = 0.5$ for (a) case 10 without control and (b) case 11 with control. Black is $v \leqslant -4.5 \times 10^{-5}$ and white is $v \geqslant 5.5 \times 10^{-5}$. The control is applied in $x \in [75, 225]$.

stream of where the perturbations are introduced in the flow. The initial flow field for the simulation was one with fully developed cross-flow vortices where the control was turned on instantaneously and after some transient behaviour of the flow and the control a steady state was obtained. The stationary flow is well-resolved with the present resolution since the perturbation levels are substantially lower than in the uncontrolled case. The solid line in figure 11 shows the energy in the $\beta = 0.25$ mode for this case. The perturbation is efficiently reduced by the control but new cross-flow vortices start to develop downstream of the control region as could be expected for this type of inflectional instability. Studying the five lowest β modes in figure 12(b) shows that the controller efficiently reduces the energy of all these modes. The control velocity on the wall is plotted for one spanwise location at $z = 0$ in figure 13(a) showing a regular sinusoidal signal with a maximum amplitude in the beginning of the control interval. The control region is then, case 14, moved further downstream centred at $x = 220$ where $\psi = 50.72^\circ$ and $\delta^* = 1.1723$. The control is

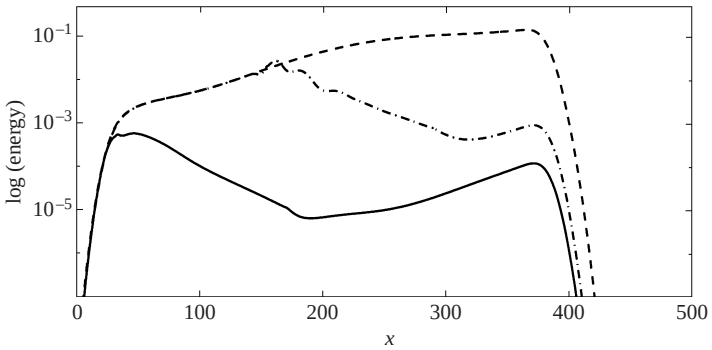

FIGURE 11. Energy growth of uncontrolled perturbation and effect of applied control in spatial DNS for $\beta = 0.25$. Dashed: case 12, uncontrolled. Solid: case 13, controlled with $\ell = 10^2$ and $r^2 = 0$ in the interval $x \in [25, 175]$ centred at $x = 100$. Dash-dot: case 14, controlled with $\ell = 10^2$ and $r^2 = 0$ in the interval $x \in [145, 295]$ centred at $x = 220$.

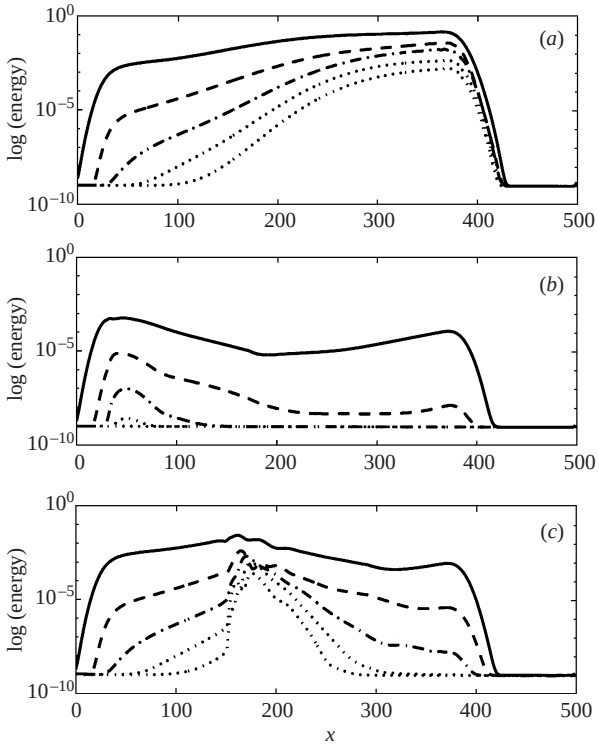

FIGURE 12. The energy in the five lowest β modes from simulations with a strong stationary perturbation for (a) case 12, uncontrolled; (b) case 13, control in $x \in [25, 225]$ and (c) case 14, with control in $x \in [145, 295]$.

allowed to act in the interval $x \in [145, 295]$. In the simulation a laminar flow with the stationary perturbation at the beginning of the domain was used as initial flow field. Then when the perturbation reaches the control region the controller reacts to stabilize the flow. This is easier than starting with the fully developed perturbation since the transients when the control is turned on are strong in this case and the time step in the simulation will be short. At the region where control is applied, the vortices

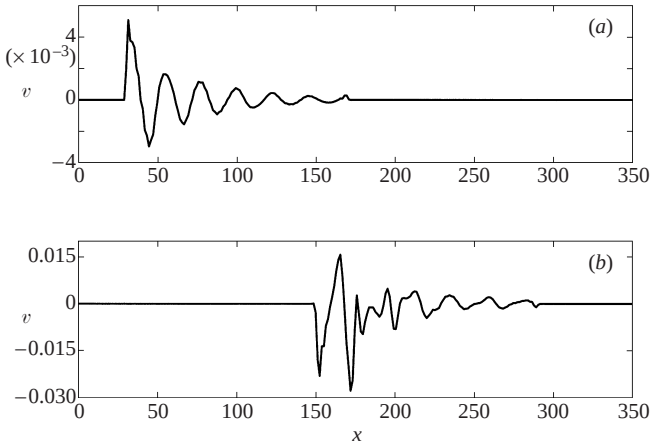

FIGURE 13. The normal velocity on the wall at $z = 0$ in the controlled cases with stationary perturbations. (a) Case 13 with control in $x \in [25, 175]$ using a controller computed with $\ell = 10^2$ and $r^2 = 0$. (b) Case 14 with control in $x \in [145, 295]$ using a controller computed with $\ell = 10^2$ and $r^2 = 0$.

will have reached a higher amplitude than in the previous case and the nonlinear effects are stronger. The simulation is run until a stationary state is obtained and the resulting energy is shown by the dash dotted line in figure 11. Despite the nonlinearity the controller reduces the energy of the perturbation within the control interval. The energy curve has some wiggles initially where the perturbation is strongest indicating that nonlinear effects are influencing the control. The normal velocity at the wall is plotted for one spanwise position at $z = 0$, also for case 14, in figure 13(b). The control signal in this case is distorted and has no apparent deterministic structure, which probably is due to the effect of nonlinearities. The maximum amplitude, which is larger than in the upstream interval, of the control appears at the beginning of the control interval and after a few strong oscillations it decays rapidly. The control affects all wavenumbers β and a plot of the effect of the controller on the five lowest values of β in the simulation is shown in figure 12(c). In this case the higher modes appear to be amplified at the beginning of the control region before they rapidly decay. The higher energy levels in these modes is related to the shape of the control signal with the nonlinear behaviour.

7. Discussion and conclusions

It was expected based on previous work that the optimal controller could stabilize unstable temporal eigenvalues. The changes of eigenvalues and eigenvectors for control applied to TS waves and the effect of controllers on transient growth had been studied by for example Bewley & Liu (1998) for channel flow. The main question here was whether these methods were transferable to the spatially evolving flow. Even though we have made some assumptions about the physics, we have shown that the controller works very well also for spatially developing flows. The growth of TS waves could be turned into decay by applying control over the unstable interval also in the spatial case. When there was a spatial optimal perturbation for transient growth in the Blasius boundary layer, the controller made the perturbation decay slowly within the control interval. In this case it was also shown that the control is effective over a long spatial interval and not only locally where it is computed.

The flow with inflectional instability in the FSC boundary layer was stabilized by the controller for random as well as stationary perturbations. The additional spatial property of a changing direction of the mean flow did not have a significant effect on the effectiveness of the controller in this case. Even higher amplitude perturbations where nonlinear effects are present were stabilized resulting in energy decay in the controlled interval, indicating some robustness of the controller to nonlinearities, as well as to changes of the mean flow.

In summary it is demonstrated that the three main mechanisms for energy growth in boundary layers can be controlled: viscous instabilities, non-modal transient energy growth and inflectional instabilities triggered by both stationary and time-varying perturbations. It appears that it is sufficient to make use of the Orr–Sommerfeld–Squire equations when designing controllers for most types of primary instability transition scenarios. The importance of linear processes for transition as well as turbulence has been emphasized by several authors investigating these processes see e.g. Henningson (1996), Kim & Lim (2000). The strength and advantage of the present formulation of the control problem is that there is no dependence on what type of perturbation the flow is subject to and transition due to secondary instabilities should not be an issue if one can control the primary ones. One question is how effective the controllers are for preventing transition to turbulence. The present study indicates that the controllers can handle some degree of nonlinearity, and quantification of the controller performance for transition in channel flow in Högberg *et al.* (2002) shows that the transition threshold for a random noise perturbation can be increased by approximately 500% using linear control. It should be mentioned that there are also important types of instabilities not considered here, namely the absolute and global instabilities. A controller for global instabilities must probably incorporate non-parallel effects since these are crucial for their existence and this cannot be obtained using the present formulation of the control problem.

To be able to make use of this type of feedback controller in practice there is a need for a good way of estimating the state of the flow based on realizable measurement data. An estimator forcing can be computed from the linear equations as described in Högberg *et al.* (2002) and then applied to force a model of the flow using wall measurements only. The combination of an estimator and a controller is called a compensator, and provides means to control the flow based on these wall measurements. The effectiveness of the estimator and the compensator for transition in channel flow is also studied in Högberg *et al.* (2002), and a natural next step is to extend these ideas to the spatially developing boundary layer flows. To obtain a control system usable in practice there might be a need to utilize a robust control $\mathscr{H}_\infty$ design to improve the robustness of the compensator. This was studied for the linear system in Bewley & Liu (1998) and showed some different properties compared to the optimal control design which could improve the behaviour of the compensator when e.g. nonlinearities are present. In future work this possibility should be explored further and tested also in the nonlinear setting.

The authors wish to thank Professor Thomas R. Bewley for pointing us in the direction of using linear control techniques, and for cooperation in creating the foundation for the present work.

REFERENCES

Andersson, P., Berggren, M. & Henningson, D. S. 1999 Optimal disturbances and bypass transition in boundary layers. *Phys. Fluids* **11**, 134–150.

Balakumar, P. & Hall, P. 1999 Optimum suction distribution for transition control. *Theor. Comput. Fluid Dyn.* **13**, 1–19.

Berggren, M. 1995 Optimal control of time evolution systems: controllability investigations and numerical algorithms. PhD thesis, Department of Computational and Applied Mathematics, Rice University, Houston, TX 77251-1892.

Berlin, S., Wiegel, M. & Henningson, D. S. 1999 Numerical and experimental investigations of oblique boundary layer transition. *J. Fluid Mech.* **393**, 23–57.

Bewley, T. R. 2001 Flow control: new challenges for a new renaissance. *Prog. Aero. Sci.* **37**, 21–58.

Bewley, T. R. & Liu, S. 1998 Optimal and robust control and estimation of linear paths to transition. *J. Fluid Mech.* **365**, 305–349.

Bewley, T. R., Moin, P. & Temam, R. 2001 DNS-based predictive control of turbulence: an optimal benchmark for feedback algorithms. *J. Fluid Mech.* **477**, 179–225.

Breuer, K. S., Haritonidis, J. H. & Landahl, M. T. 1989 The control of transient disturbances in a flat plate boundary layer through active wall motion. *Phys. Fluids* A **1**, 574–582.

Cathalifaud, P. & Luchini, P. 2000 Algebraic growth in boundary layers: optimal control by blowing and suction at the wall. *Eur. J. Mech.* B Fluids **19**, 469–490.

Cooke, J. C. 1950 The boundary layer of a class of infinite yawed cylinders. *Proc. Camb. Phil. Soc.* **46**, 645–648.

Gad-el-Hak, M. 1996 Modern developments in flow control. *Appl. Mech. Rev.* **49**(7), 364–379.

Hanifi, A., Schmid, P. J. & Henningson, D. S. 1996 Transient growth in compressible boundary layer flow. *Phys. Fluids* **8**, 826–836.

Henningson, D. S. 1996 Comment on 'Transition in shear flows. Nonlinear normality versus non-normal linearity' [*Phys. Fluids* **7**, 3060 (1995)]. *Phys. Fluids* **8**, 2257–2258.

Högberg, M. 2001 Optimal control of boundary layer transition. TRITA-MEK 2001: 13, PhD thesis, Department of Mechanics, Royal Institute of Technology (KTH), S-100 44 Stockholm, Sweden http://www.mech.kth.se.

Högberg, M. & Bewley, T. R. 2000 Spatially localized convolution kernels for feedback control of transitional flows. In *Proc. 39th IEEE Conf. on Decision and Control*, vol. 4, pp. 3278–3283.

Högberg, M., Bewley, T. R. & Henningson, D. S. 2002 Linear feedback control and estimation of transition in plane channel flow. Submitted to *J. Fluid Mech.*

Högberg, M. & Henningson, D. S. 1998 Secondary instability of cross-flow vortices in Falkner–Skan–Cooke boundary layers. *J. Fluid Mech.* **368**, 339–357.

Hulsing, K. P. 1999 Methods for computing functional gains for LQR control of partial differential equations. PhD thesis, Virginia Polytechnic Institute and State University.

Ito, K. & Morris, K. A. 1998 An approximation theory of solutions to operator Riccati equations for $\mathscr{H}^\infty$ control. *SIAM J. Control optim.* **36**, 82–99.

Jacobson, S. A. & Reynolds, W. C. 1998 Active control of streamwise vortices and streaks in boundary layers. *J. Fluid Mech.* **360**, 179–211.

Jameson, A. 1989 Computational aerodynamics for aircraft design. *Science* **245**, 361–371.

Joshi, S. S., Speyer, J. L. & Kim, J. 1997 A systems theory approach to the feedback stabilization of infinitesimal and finite-amplitude disturbances in plane Poiseuille flow. *J. Fluid Mech.* **332**, 157–184.

Joslin, R. D., Gunzburger, M. D., Nicolaides, R. A., Erlebacher, G. & Hussaini, M. Y. 1997 A self-contained, automated methodology for optimal flow control. *AIAA J.* **35**, 816–824.

Kawakami, M., Kohama, Y. & Okutsu, M. 1999 Stability characteristics of stationary crossflow vortices in three-dimensional boundary layer. *AIAA Paper* 99-0811.

Kim, J. & Lim, J. 2000 A linear process in wall-bounded turbulent shear flows. *Phys. Fluids* **12**, 1885–1888.

Kozlov, V. V. & Grek, G. R. 2000 Stationary and nonstationary streaky structures and secondary instability of boundary layers. In *Laminar-Turbulent Transition, Proc. IUTAM Symposium, Sedona, Arizona, USA* (1999) (ed. H. Fasel & W. Saric). Springer.

Laub, A. J. 1991 Invariant subspace methods for the numerical solution of Riccati equations. In *The Riccati Equation* (ed. Bittaini, Laub & Willems), pp. 163–196. Springer.

Lerche, T. 1997 Experimentelle Untersuchung nichtlinearen Strukturbildung im Transitionsprozeß einer instabilen Grenzschicht. *Fortscrittberichte, VDI, Reihe 7: Strömungstechnik*, Nr. 310.

Luchini, P. 2000 Reynolds-number-independent instability of the boundary layer over a flat surface: optimal perturbations. *J. Fluid Mech.* **404**, 289–309.

Lumley, J. & Blossey, P. N. 1998 Control of turbulence. *Annu. Rev. Fluid Mech.* **30**, 311–327.

Lundbladh, A., Berlin, S., Skote, M., Hildings, C., Choi, J., Kim, J. & Henningson, D. S. 1999 An efficient spectral method for simulation of incompressible flow over a flat plate. *Tech. Rep. Department of Mechanics, KTH, TRITA-MEK* 1999: 11.

Malik M. R., Li, F., Choudhari, M. M. & Chang, C.-L. 1999 Secondary instability of crossflow vortices and swept-wing boundary-layer transition. *J. Fluid Mech.* **399**, 86–115.

Metcalfe, R. W. 1994 Boundary layer control: A brief review. In *Computational Fluid Dynamics '94, Invited Lectures of the Second European CFD Conference; Stuttgart, Germany* (ed. S. Wagner, J. Periaux & E. Hirschel), pp. 52–60. John Wiley & Sons.

Mughal, M. S. 1998 Active control of wave instabilities in three-dimensional compressible flows. *Theor. Comput. Fluid Dyn.* **12** 195–217.

Müller, B. & Bippes, H. 1988 Experimental study of instability modes in a three-dimensional boundary layer. *AGARD-CP* 438, No. 18.

Nordström, J., Nordin, N. & Henningson, D. S. 1999 The fringe region technique and the Fourier method used in the direct numerical simulation of spatially evolving viscous flows. *SIAM J. Sci. Comput.* **20**, 1365–1393.

Pralits, J. O., Hanifi, A. & Henningson, D. S. 2001 Adjoint-based optimization of steady suction for disturbance control. Part 1. Incompressible flows. In *Towards Optimal Design of Vehicles with Low Drag: Applications to Sensitivity Analysis and Optimal Control*. Licenciate thesis of Jan Pralits, Department of Mechanics, Royal Institute of Technology, Stockholm, Sweden *TRITA-MEK* 2001: 07.

Saric, W. S., Carrillo, R. B. Jr & Reibert, M. S. 1998 Leading-edge roughness as a transition control mechanism. *AIAA Paper* 98-0781.

Schlichting, H. 1979 *Boundary-layer Theory*, 7th edn. McGraw-Hill.

Skelton, R. E. 1988 *Dynamic Systems Control, Linear Systems Analysis and Synthesis*. John Wiley & Sons.

Thomas, A. S. W. 1990. Active wave control of boundary-layer transition. In *Viscous Drag Reduction in Boundary Layers* (ed. D. M. Bushnell & J. N. Hefner). Progress in Astronautics and Aeronautics, vol. 123. AIAA.

Walther, S., Airiau, C. & Bottaro, A. 2001 Optimal control of Tollmien–Schlichting waves in a developing boundary layer. *Phys. Fluids* **13**, 2087–2096.

Wassermann, P. & Kloker, M. 2000 DNS-investigations of the Development and Control of Crossflow Vorticies in a 3D Boundary-layer Flow. In *Laminar-turbulent Transition, Proc. IUTAM Symposium, Sedona, Arizona, USA* (1999) (ed. H. Fasel & W. Saric). Springer.

Weideman, J. A. C. & Reddy, S. C. 2000 A Matlab differentiation matrix suite. *ACM Trans. of Math. Software* **26**, 465–519.

White, E. B. & Saric, W. S. 2000 Application of variable length leading-edge roughness for transition control on swept wings. *AIAA Paper* 2000-0283.